© 2008. Astronomical Society of Japan.

AKARI/IRC Deep Survey in the North Ecliptic Pole Region

Takehiko Wada,[1,*] Hideo Matsuhara,[1] Shinki Oyabu,[1] Toshinobu Takagi,[1] Hyung Mok Lee,[2]
Myungshin Im,[2] Youichi Ohyama,[3] Tomotsugu Goto,[4] Chris P. Pearson,[5,6] Glenn J. White,[7,5]
Stephen Serjeant,[7] Kensuke Wada,[8,1] and Hitoshi Hanami[9]

[1]*Institute of Space and Astronautical Science, Japan Aerospace Exploration Agency,*
3-1-1 Yoshinodai, Sagamihara, Kanagawa 229 8510

[2]*Department of Physics & Astronomy, FPRD, Seoul National University, Shillim-Dong, Kwanak-Gu, Seoul 151-742, Korea*

[3]*Institute of Astronomy and Astrophysics, Academia Sinica, P.O. Box 23-141, Taipei 10617, Taiwan*

[4]*Institute for Astronomy, University of Hawaii, 2680 Woodlawn Drive, Honolulu, HI 96822, USA*

[5]*Rutherford Appleton Laboratory, Oxon, OX11 0QX, UK.*

[6]*Department of Physics, University of Lethbridge, 4401 University Drive, Lethbridge, Alberta T1J 1B1, Canada*

[7]*Department of Physics & Astronomy, The Open University, Milton Keynes, MK7 6AA, UK*

[8]*Department of Physics, Tokyo Institute of Technology, 2-12-1 Ookayama, Meguro, Tokyo 152-8551*

[9]*Iwate University, 3-18-8 Ueda, Morioka, Iwate 020-8550*

Abstract

We have made a deep and wide imaging survey with all nine AKARI/IRC bands from 2 to 24 μm within a half degree of the North Ecliptic Pole. The survey covered a circular area of 0.38 deg^2 centered at RA = 17^{h}56^m, Dec = 66°37′ where a deep optical multi-band survey has been conducted by Subaru/Suprime-Cam. The 5 σ sensitivity of the survey for point sources is 11.0, 48, 117, and 275 μJy at wavelengths 3, 7, 15, and 24 μm, respectively. The survey is limited by sky noise at wavelengths from 7 to 24 μm, and limited by source confusion from 2 to 4 μm. We have also made a point source catalog at each band, consisting of more than 5000 sources with a 50% completeness limit of 93 μJy at 15 μm. Our results are consistent with the pilot survey at faint fluxes and has better statistical significance at the bright fluxes. This is the first near- and mid-infrared sub-mJy extragalactic survey with contiguous wavelength coverage from 2 to 24 μm and a large band-merged catalogue. It will provide powerful and unique diagnostics of obscured star-formation and AGN activities in the galaxies up to $z = 2$.

Key words: galaxies : evolution — galaxies : statistics — infrared galaxies — space vehicles: instruments

1. Introduction

The year 2008 marks the 25th anniversary of the first infrared astronomical satellite, IRAS (Neugebauer et al. 1984), which revealed the presence of optically faint, but infrared luminous, dust-obscured galaxies (Luminous Infrared Galaxies: LIRGs) through the first all-sky survey at mid- and far-infrared wavelengths. Subsequent infrared space missions, such as ISO (Kessler et al. 1996) and Spitzer Space Telescope (Werner et al. 2004) have led us to obtain enormous data sets on star-forming galaxies and active galactic nuclei (AGN), both of which may be obscured by dust (Genzel & Cesarsky 2000; Franceschini et al. 2006 and references therein). Most recently, AKARI was launched on 2006 February 21 (Murakami et al. 2007). Following the orbit maneuvers, the lid-opening on April 13, and the initial checkout operations, the routine-phase observations with AKARI started on May 8. The mid- and far-IR observations finished on 2007 August 26 when the liquid helium ran out, while the near-infrared observations are still ongoing.

AKARI has performed the following three major extra-galactic surveys (Matsuhara et al. 2006):

- a deep 2.4–24 μm survey at the North Ecliptic Pole (NEP), covering a 0.4 deg^2 circular area (NEP-Deep);
- a wide and shallow 2.4–24 μm survey at the NEP, covering a 5.8 deg^2 circular area surrounding the NEP-Deep field (NEP-Wide);
- a deep 60–160 μm survey towards a low-cirrus region near the South Ecliptic Pole (SEP), covering a 11 deg^2 fan-shape field (AKARI Deep Field South: ADF-S).

NEP-Deep and NEP-Wide have been conducted in the AKARI Large-area Survey (LS) "LSNEP" (PI: Matsuhara), and the far-IR survey has been conducted in the AKARI Mission Program (MP) "FBSEP" (PI: Matsuura).

This paper describes the NEP-Deep survey, while Lee et al. (2008) and M. Shirahata et al. (2008 in preparation) describe the NEP-Wide and ADF-S surveys, respectively. In order to understand the nature of the sources detected, the NEP-Deep field has been also surveyed at other wavelengths (see table 1).

As with the various deep extra-galactic surveys with Spitzer telescope, the major scientific goals of the AKARI extra-galactic surveys are to unveil the cosmic star-formation history obscured by dust, to understand the link between the AGNs and the LIRGs, and to comprehend stellar mass assembly in the universe through the survey of large cosmic volume out to $z \sim 3$.

---

* Further information contact Takehiko Wada (wada@ir.isas.jaxa.jp).

Table 1. Summary of NEP-Deep multi-wavelength surveys.

| Observatory	Band / Filter	Area / Target	Sensitivity	Status
AKARI/FIS	60–160 μm 4 bands	1 deg^2	~ 20 mJy	analyzed
AKARI/IRC	2.5–24 μm 9 bands	0.4 deg^2	60 μJy @ 15 μm	analyzed
	Slit-less spectroscopy (2–11, 17–24 μm)	0.25 deg^2	0.5 mJy @ 10 μm	analyzed
Subaru/Suprime-Cam	$BVRi'z'$, $NB\,711$	$27' \times 34'$	$B = 28$ AB	paper in preparation
Subaru/FOCAS	optical spectroscopy	57 sources in NEP	$R \sim 24$ AB	analysis ongoing
KPNO-2.1 m/Flamingos	J, $K_{\rm s}$	$25' \times 30'$	$K_{\rm s} = 20$ Vega	published*
CFHT/MegaCam	$g'r'i'z'$	2 deg^2	$g'r'i' \sim 26$ AB	published†
	u'	2 deg^2	~ 26 AB	observed
GALEX	NUV, FUV	$0°\!.6\ \phi$	NUV $= 26$	obs. ongoing
WSRT	20 cm	1 deg^2(partial overlap)	$\sim 100\,\mu$Jy	analyzed
VLA-archive	10 cm	$1°\!.5\ \phi$	$200\,\mu$Jy	archived
GMRT	610 MHz	$40'\ \phi$	60–80 μJy	observed
SCUBA-2	850 μm	1 deg^2	8 mJy (10 σ)	to be obs.
	450 μm	0.02 deg^2	~ 20 mJy (confusion limit)	to be obs.

* Imai et al. (2007).
† Narae et al. (2007).
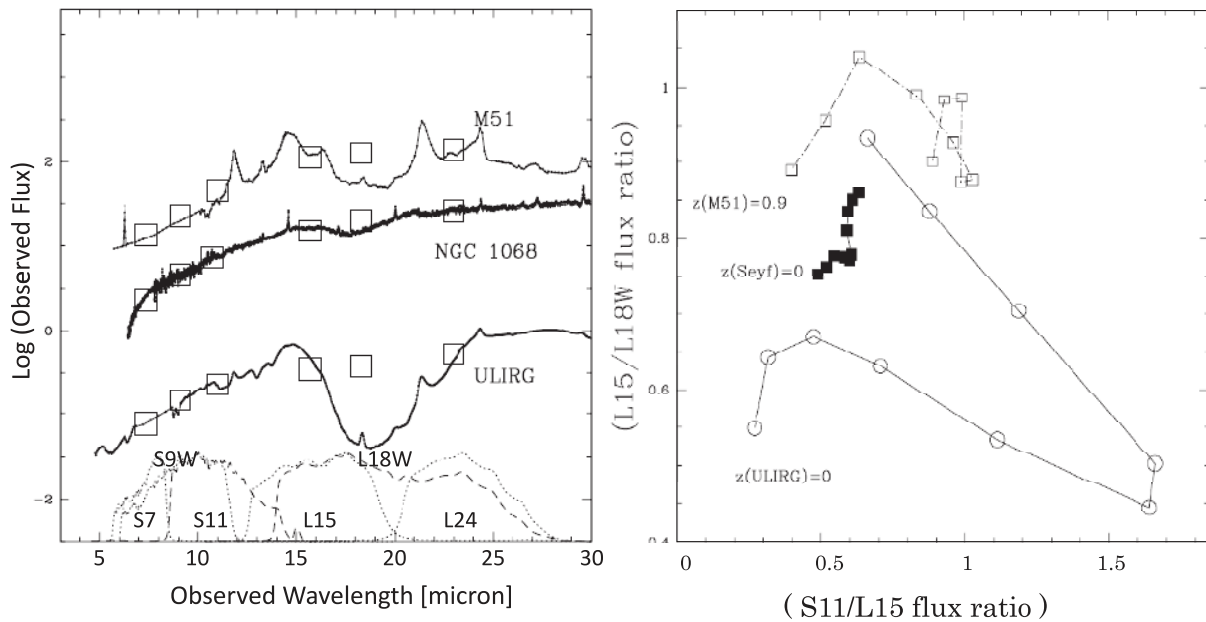
Fig. 1. Left: Mid-infrared SEDs of M 51 (an example quiescent galaxy), NGC 1068 (an example AGN), and Arp 220 (a star-forming ULIRG). The spectral coverage of the AKARI/IRC imaging bands are indicated by dotted and dashed lines. Right: The mid-infrared color–color diagram of these template objects from redshifts $z = 0$ to 0.9, in 0.1 steps. Note the clear separation of the SEDs in this figure (Malkan et al. 2008, private communication).

These scientific topics, however, have already been addressed with multi-wavelengths surveys including the mid- and far-infrared observations with Spitzer, which offers excellent sensitivities in the four IRAC wave-bands between 3.6 and 8.0 μm (Fazio et al. 2004) and at MIPS 24 μm (Rieke et al. 2004). For example, based on a 24 μm selected sample, Le Floc'h et al. (2005) estimated the evolving 7 μm luminosity function at $z = 0$–1, while Caputi et al. (2006) and

Franceschini et al. (2006) discussed the cosmic star-formation history obscured by dust at $z = 1$–2, reporting that the star-formation activity of massive galaxies ($M \geq 10^{11}\,M_\odot$) at $z \sim 2$ was a hundred times larger than the present. These ultra-luminous ($L \geq 10^{12}\,L_\odot$) infrared galaxies (ULIRGs) may be the progenitors of present-day massive galaxies. Pérez-González et al. (2008) (and references therein) discussed the evolution of the stellar mass function of the universe based

on IRAC 3.6 and 4.5 μm selected sample, and revealed that the "down-sizing" picture was also present in the stellar mass function evolution.

One should note, however, that the estimation of the star-formation rate of distant ($z > 1$) dusty galaxies mostly relies on the single MIPS 24 μm photometry of the sample. This may result in incomplete sampling of dusty massive galaxies especially at $z \sim 1.5$, at which ULIRGs with strong silicate absorption become very faint in the 24 μm band (Takagi & Pearson 2005). This can clearly be seen in the redshift distribution of 24 μm selected sources (Caputi et al. 2006; Franceschini et al. 2006). Moreover, the strong 6.2 and 7.7 μm PAH features prominent in the mid-infrared spectra of star-forming galaxies can enter the MIPS 24 μm passband only at $z > 2$.

The wavelength coverage of AKARI/IRC (Onaka et al. 2007) between 8 and 24 μm (the gap between the IRAC and MIPS onboard Spitzer) is especially useful for obtaining complete samples of dusty ULIRGs at $z \sim 1$–1.5. As shown in figure 1, galaxies with bright PAH emission or deep silicate features have distinct mid-infrared colors, and are clearly separated from AGNs or quiescent galaxies. Deep surveys with AKARI/IRC are not only important for obtaining a reliable selection of high-z ULIRGs, but also enable us to identify power-law objects, which are candidate dust-obscured AGNs (see Alonso-Herrero et al. 2006). Although Spitzer/IRS (Houck et al. 2004) has an imaging capability at 16 μm in its peak-up mode, its relatively small field of view (1.2 arcmin^2) is unsuitable for undertaking wide-field, deep mapping projects like the AKARI NEP surveys.

As a pilot study for a full analysis of the NEP survey, we reported first results from a small (50–100 arcmin^2) subset of the NEP survey : Lee et al. (2007) provided the first insights on the 11 μm selected sample, Wada et al. (2007) reported initial results of the deep 15 μm survey and Matsuhara et al. (2007) provided their optical identifications. Takagi et al. (2007) reported optical–mid-infrared spectral characteristics of the first 18 μm selected sample.

In this paper, we mainly focus on the NEP-Deep survey description. In section 2, we describe the strategy of the spacecraft/instrument operation, and the performance of the pointed observations for mapping the field. The details of image data reduction and the resulting images are presented in section 3. In section 4, we describe the source extraction and the resulting source catalog, and the estimation of sensitivities will be presented in section 5. In section 6, we briefly discuss the source number counts and the achieved sensitivities derived by our methods, and the prospects for the improvement. Section 7 gives the summary of the paper.

2. Observations

2.1. NEP-Deep Survey Strategy with AKARI/IRC

The scientific requirements for the survey area and the number of pointed observations (depth) were described in Matsuhara et al. (2006) based on the pre-launch expectation of the sensitivities.

An area of 0.5–1 deg^2 is required for the survey area in order to reduce the effect of the cosmic variance for $z = 1$–3 universe, and a depth of ten pointed observations per field-of-view (FOV)

is required in the mid-infrared bands in order to detect ULIRGs at $z = 2$–3. All nine IRC bands are required for secure distinction between AGN and star-formation and for the determination of photometric redshifts by SED fitting (e.g., Negrello et al. 2008). In total, 504 pointed observations were planned to cover the 0.5 deg^2 area for the NEP-Deep survey in the 1.5 year of mission life. The pointing opportunities for the NEP-Deep survey were subsequently reduced to 266, following a reconsideration of the AKARI observing program in the light of the predicted liquid helium life time (1 year including the two months checkout phase) in the initial checkout. In order to maintain the benefit of the wide field, we decided to reduce the number of pointed observations per FOV from 10 to 4. The reduction of the number of pointed observations together with the stray light problem from the Earth shine, which is described later, degrades the sensitivity by a factor of 5 from the pre-launch prediction (from 22 μJy to 117 μJy at 15 μm, for example). The survey depth for a ULIRG with a luminosity of $3 \times 10^{12} L_\odot$ at 15 μm, for example, will be degraded from a redshift of $z = 2$ to 1.5 as a consequence (Matsuhara et al. 2006).

There are strong technical constraints on the pointing direction imposed by the orbit and the design of the mission (Murakami et al. 2007). First, there is only $\pm 0°.6$ freedom in solar elongation, i.e., only a strip area with a width of $1°.2$ and a length of $360°$ through North and South Ecliptic Poles is visible in any given moment. This is due to design of the Sun shield and the attitude determination system. The solar elongation of the telescope boresight is always $90°$ in the spacecraft's nominal attitude, and the offset control is restricted to $< 0°.6$ in either direction. Because of this limitation, the continuous viewing zone, in which AKARI can make pointed observations at any season, is limited to the two circular areas with a radius of $0°.6$ at the NEP and the SEP. All other regions have an observational window once every six months as the sun's direction changes in geocentric coordinates. The duration of each window is proportional to the secant of the ecliptic latitude. The visibility is at a minimum for a source on the ecliptic plane: for these objects, there are only 1.2 days in which observations are possible every six months. Second, the duration of the integration time in one pointed observation is limited to ten minutes, due to the orbit. This is a low Earth orbit with an altitude of 700 km, so the duration of any single pointed observation is limited to 15 minutes in order to prevent the Earth shine from illuminating the telescope baffle. A few minutes are also required for pointing stabilization. Third, no large area survey is possible with pointed observations in the low visibility area (i.e., low ecliptic latitudes), because of the requirement to have redundant observations in the primary mission of AKARI, the All-Sky Survey. Therefore, the two major large area surveys using pointed observations (LSNEP and LSLMC) took place in the ecliptic pole regions where AKARI has very good visibility. Existing deep survey fields such as COSMOS (Scoville et al. 2007: $\beta = -9.36$), SXDS (Furusawa et al. 2008: $\beta = -17.7$), SDF (Kashikawa et al. 2004: $\beta = -33.4$), GOODS-N/S (Giavalisco et al. 2004: $\beta = 57.3$ and $\beta = -45.2$), and ELAIS-N2 (Oliver et al. 2002: $\beta = 62.0$) could not be selected as major AKARI survey fields because of their low visibilities.
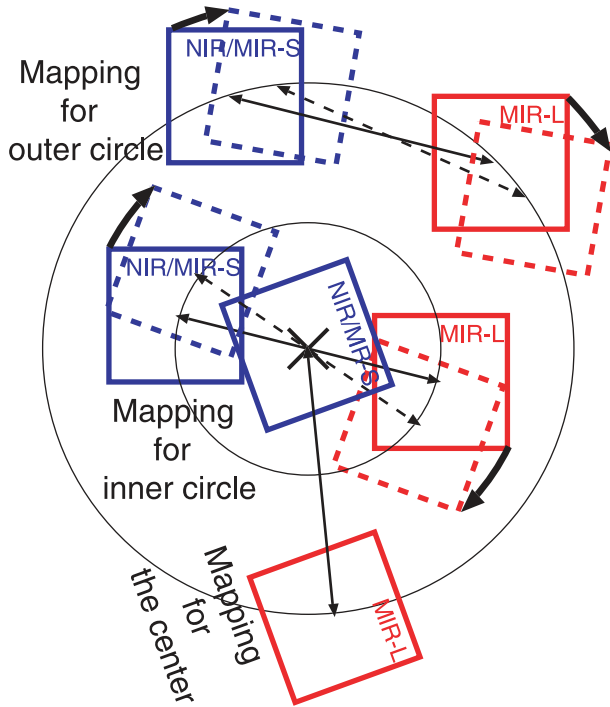
Fig. 2. The mapping strategy in this survey. Further details are discussed in the text.

There are also strong constraints on the tiling of FOVs. First, the FOV of the MIR-L channel is separated by approximately 20′ from that of the NIR and MIR-S channels of AKARI/IRC, although the three channels take images simultaneously. Second, the position angle of IRC FOVs is determined by the date of the observation. No roll angle control is permitted because of satellite operations.

Since each sky position was to be covered with multiple pointed observations, we selected Astronomical Observational Template (AOT) AOT05 in which no changing of filter and no dithering of telescope position during one pointed observation is performed, resulting in the maximum observational efficiency compared to the other AOTs.

In order to maximize the area which is covered by all the IRC band, and in order to maintain an approximately uniform depth across the survey area in each band (4 pointed observations per FOV per filter or more), special care has been taken in observation planning. As shown in figure 2 and figure 3, the observation maps were made of three sets of pointed observations: the central region, the inner circular region, and the outer circular region.

In the central region (RA = 17^h56^m, Dec = $66°37′$), 30 pointed observations in total were planned in order to make 5 pointed observations for each of the three filters in both the NIR/MIR-S and MIR-L channels. Two pointed observations for each three filters for MIR-L channel and one pointed observation for NIR/MIR-S channels, which were planned according to the pre-flight limit of the offset control ($\pm 1°0$), were canceled in the final scheduling of the observations because of the in-flight limit of the offset control ($\pm 0°6$). In total, 23 pointed observations were successfully completed.
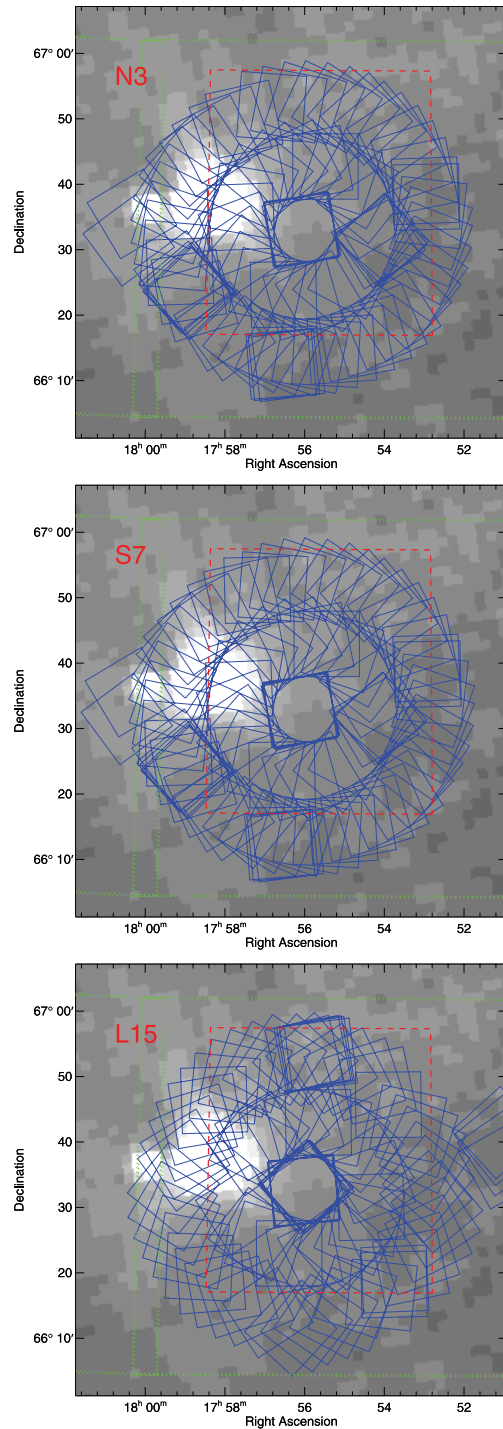
Fig. 3. The distribution of the FOVs. The boxes show the position and inclination angle of the FOVs for each pointed observation in this survey. Cases for *N3*, *S7*, and *L15* bands, in which images are taken simultaneously, are shown for example. The distribution of the FOVs in the *N3* and *S7* bands are almost identical because NIR channel (*N3*) and MIR-S channel (*S7*) share the same FOV by a beam splitter. MIR-L channel (*L15*) looks at the field 20′ apart from the FOVs of the NIR/MIR-S channel. The final mapping area in the *L15* band image, however, are almost identical to those of the *N3* and *S7* band images, as a result of careful mapping plan shown in figure 2. The background image is the IRAS 25 μm map. The FOVs of the Subaru/Suprime-Cam observation (dashed line) and the CFHT/MegaCam survey (dotted line) are also shown.

During the observations of the central regions, the other channels were directed at the outer circular regions and these bonus data are incorporated into the mosaicked image.

The inner circular region was constructed such that the midpoint between the NIR/MIR-S and MIR-L channels was always located at the center of the field. Because the separation of the NIR/MIR-S and MIR-L channels is 20′, the radius of the inner circle is set to 10′. The NIR/MIR-S and MIR-L channels observe opposite sides of the circle. As the direction of the Sun changes in geocentric coordinates, the position of NIR/MIR-S also traverses the circle, as does the MIR-L channel. A region observed with the NIR/MIR-S (or MIR-L) channel will be observed with MIR-L (or NIR/MIR-S) after six months. In one year, the entire inner circle is observed with both the NIR/MIR-S channels and the MIR-L channel. One observation every 18 days has been conducted for each of the three filters, and 63 pointed observations have been done for the inner circular region in total. All three IRC channels operate simultaneously; therefore three observations, with a filter change in each observation, is enough to obtain data in all nine filter bands across the whole region.

The outer circular region was covered in the following manner. First, the radius of the outer circle was set to 20′, so that there would be no gap between the inner and outer circular regions. Second, pointed observations using the NIR/MIR-S channel were located on the outer circle, so that the MIR-L channel would also be located on the outer circle (20′ apart from the NIR/MIR-S channels). Because the position angle of the IRC FOV is determined only by the date of the observations, there are only two solutions of this geometry for each date. One observation in every 7.5 days has been done for each of three filters, and 146 pointed observations have been done for the outer circular region in total. The radius of the outer circle is set to 20′, and the separation between NIR/MIR-S and MIR-L channels is also 20′, so the angle between the channels measured from the center of the field is 60°. Because the direction of the Sun changes one degree per day, any region which is observed with NIR/MIR-S or MIR-L channel can be observed by the other channel 60 days later.

Both the inner and outer circular region observations were planned within the strict constraints of observatory scheduling. From April to August, the observations near the NEP were affected by stray light from Earth shine, and the corresponding pointed observations (north-east side of the outer circular region) in the MIR-L channel consequently had lower signal to noise ratio. This region has a lower value in the weight map in figure 4.

Some pointed observations in the westernmost part of the outer circle were beyond limits of ± 0°.6 offset control and not observed. The places in the inner circle which exceeded the 0°.6 offset control limit were covered in 2007 August with an additional allocation of 34 pointed observations.

2.2. Performance of the Observations

The observations were executed from 2006 May to 2007 August, as a part of the large area survey program, LSNEP. AKARI observations are classified into two phases. Phase 1 lasted from 2006 May to 2006 November. In phase 1, AKARI dedicated most telescope time to the All-Sky Survey,

and limited the number of pointed observations to high visibility regions (near the ecliptic poles). Phase 2 started in 2006 November, in which most pointed observations were performed. The observations of LSNEP were performed in both phases 1 and 2.

The data sets used for NEP-Deep can be identified as follows. All AKARI/IRC pointed observations have an identification number which consists of 7 digits. The first three digits indicate the AKARI program IDs and the next four digits indicate an identification number within the program. Because NEP-Deep is a part of LSNEP, all data taken for NEP-Deep have the AKARI Program IDs of LSNEP: 210 for phase 1 or 211 for phase 2. The data sets which have an identification number starting with 0 indicate the original planned observations, while those starting with 1 indicate additional observations in 2007 August. LSNEP includes both the NEP-Deep and NEP-Wide observations. The remaining three digits can be used to distinguish Deep from Wide, because all the NEP-Deep observations have a value less than 505 while the NEP-Wide observations have values equal to or greater than 505.

3. Reduction of the Image Data

The data reduction for each pointed observation, such as dark subtraction, subtraction of scattered light inside the camera, correction for detector non-linearity, flat fielding, and correction for distortion, was performed by using the IRC imaging pipeline version 20071017.[1] We also performed a removal of the diffuse background by subtracting the median filtered self-image from the MIR-S and MIR-L observations.

Astrometry in all NIR filters, the $S7$ and the $S9W$ images was done automatically by the IRC imaging pipeline by registering the point source positions against the Two Micron All-Sky Survey (2MASS: Skrutskie et al. 2006). However, the astrometry of the MIR-S $S11$ and all MIR-L bands images was not successful due to the lack of a sufficient number of sources cross-matched with the 2MASS catalog. This is probably because galactic main sequence stars, which have relatively blue color in the near- and mid-infrared wavelengths, dominate the 2MASS catalog, while extra-galactic sources, which have comparatively red colors at these wavelengths, are predominant in the MIR-S and MIR-L catalogs. The astrometry at the longer wavelengths images was therefore derived automatically by cross-matching with sources detected in the shorter wavelength images. The astrometry of $S11$ was derived from the $S9W$ source catalog, $L15$ was derived with $S11$, $L18W$ with $L15$, and that of $L24$ was done with the $L18W$ source catalog. For a few images, especially in the longer wavelength bands, the astrometry could not be computed with this procedure. For these data, the astrometry was done by cross-matching by hand.

There were some data excluded from the final analysis for several reasons. One major reason is the non-uniform background caused by the Earth shine, which is found in the data taken from April to August, especially in MIR-S and MIR-L. The pipeline has an algorithm which removes the diffuse background by subtracting a median filtered image. In some pointed

---

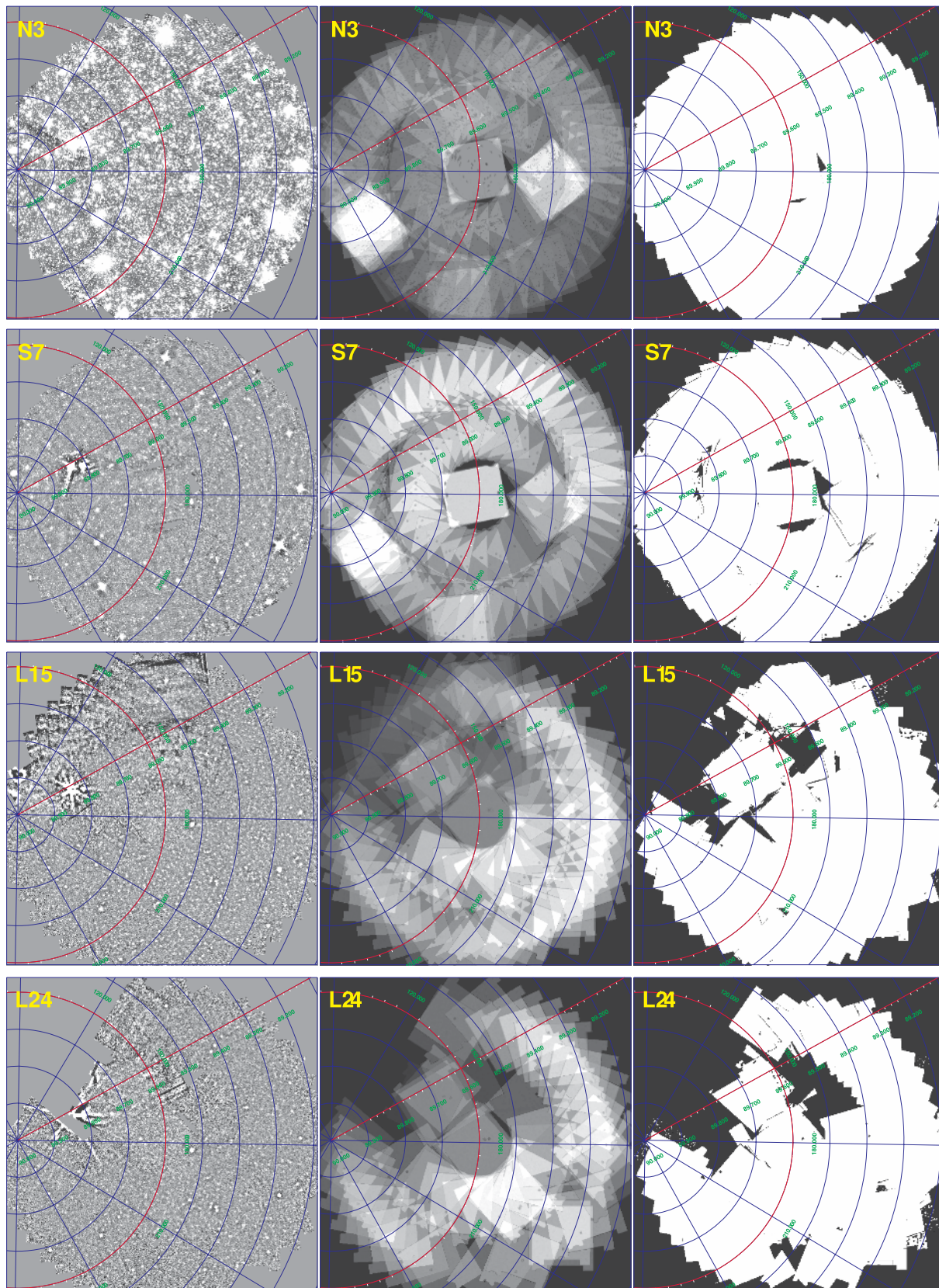[1] AKARI IRC Data User Manual ⟨http://www.ir.isas.jaxa.jp/AKARI/Observation/DataReduction/IRC/⟩.

Fig. 4. The final mosaicked images (left) and the corresponding weight maps are shown (mid). The right figure shows areas used for point source extraction and estimation of sky noise and completeness. All figures are shown in equatorial coordinates. Only *N3*, *S7*, *L15*, and *L24* band images are shown for example.
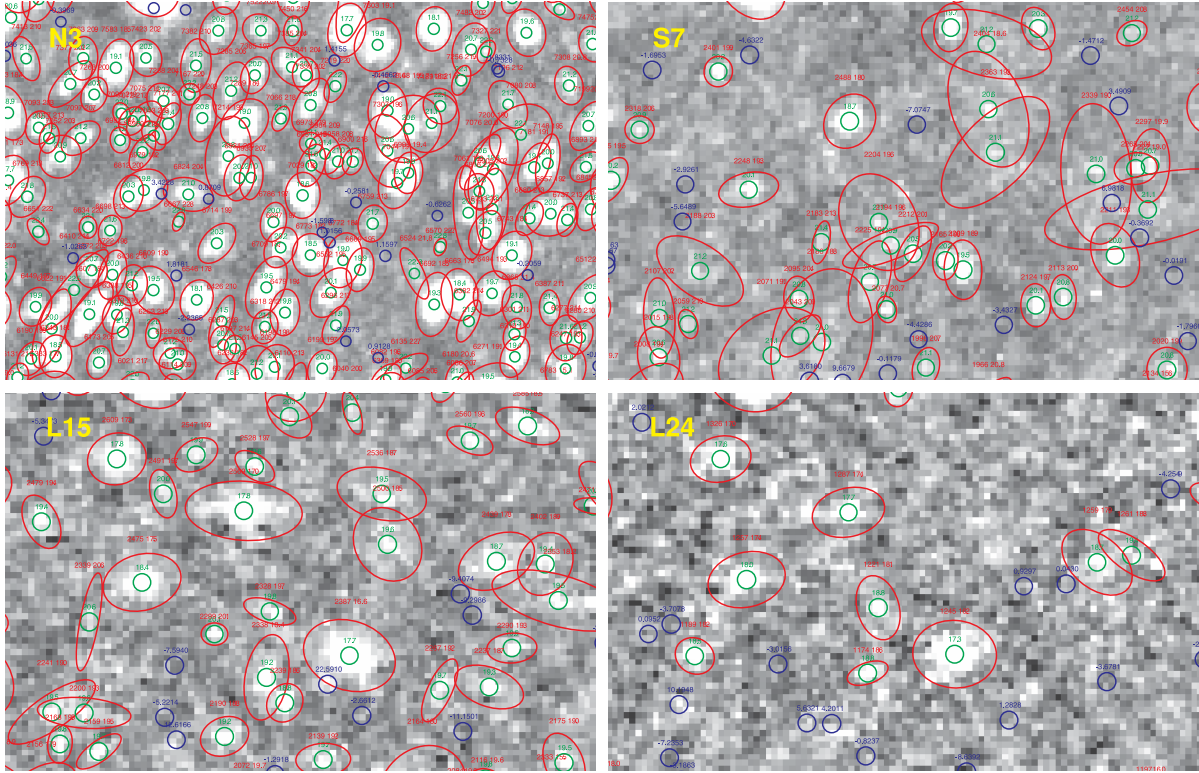
Fig. 5. Close up views of the AKARI/IRC for each band image. The green circles indicate the positions of detected sources. The MAGAUTO apertures (red) are superposed on each AKARI source. The blue circles indicate the apertures on blank sky positions which were used for the calculation of the detection limit. Only *N3*, *S7*, *L15*, and *L24* band images are shown for example.

observations, however, the spatial frequency of the non-uniform background is too high to be removed by the median filter, or the background level is so high that the photon-noise caused by the background severely degrades the signal-to-noise ratio. Those data were excluded from further analysis. We also excluded the data taken in pointed observations in which the attitude of the telescope was unstable.

As a result, the numbers of available pointed observations for further analysis are 86, 89, 84, 92, 87, 87, 89, 87, and 78 in the *N2*, *N3*, *N4*, *S7*, *S9W*, *S11*, *L15*, *L18W*, and *L24* bands, respectively.

Producing one mosaic image from the pointed observations was done by the `Swarp` software[2], which combines images into one common frame applying appropriate coordinate transformation using their astrometric information. The `Swarp` software also produces the weight map, which can be used for image quality assessment.

In order to remove spurious data, images were combined by taking median value of the data among the image to be stacked for each pixel in the final mosaic image. The final mosaicked images, together with the weight maps for each band, are shown in figure 4. We also present a close-up view of the final mosaic images in figure 5 to demonstrate the image quality.

4. Point Source Catalog

4.1. Effective Area

We have made a point source catalog at each band, in order to estimate the sensitivity of the survey. The quality of the mosaicked image is not uniform across the survey. In order to simplify the analysis, we have used the region in which the weight map has a value more than 0.1 (in case of *N2*, *N3*, *N4*, *S9W*, and *S11* bands), 0.15 (in case of *L15* and *L18W*), 0.2 (in case of *S7*), and 0.29 (in case of *L24*). The resulting sky areas used for further analysis are summarized in table 2 and figure 4.

4.2. Source Extraction and Photometry

Sextractor (Bertin & Arnouts 1996) was used for source extraction. The extraction criterion was a connection of five pixels having more than a $1.6532\,\sigma$ significance above the local sky. If the flux is equally distributed over these five pixels, it corresponds to a $5\,\sigma$ detection. The PSF has a weak concentration at its center, and the above criterion gives a slightly higher significance than $5\,\sigma$ for a point source.

The flux of each extracted source was evaluated by aperture photometry calculated in Sextractor. Elliptical aperture photometry with variable size (Sextractor's MAGAUTO) was used for the further analysis. The parameters "Kron factor" and "minimum radius" were set to the default values of 2.5 and 3.5, respectively. The apertures used for each detected source are

---

[2] Available in ⟨http://terapix.iap.fr/rubrique.php?id_rubrique=49⟩.

Table 2. Summary of the survey.

Band	Total area (arcmin^2)	Area* (arcmin^2)	$N_{\rm sources}$[†]	5 σ limit[‡] (μJy)	50% limit[§] (μJy)
N2	2099	2099	23323	14.2	42.5
N3	2123	2123	26193	11.0	34.6
N4	2080	2079	26318	8.0	29.0
S7	2093	1967	7702	48.9	54.0
S9W	2078	1539	5595	58.5	62.6
S11	2102	1443	4994	70.9	80.7
L15	2220	1654	6737	117.0	93.3
L18W	2226	1113	4189	121.4	98.8
L24	1958	1444	2813	275.8	209.8

* Used for source extraction and estimations of sky noise and completeness limit.
† Number of sources detected.
‡ Detection limit (sky noise limit).
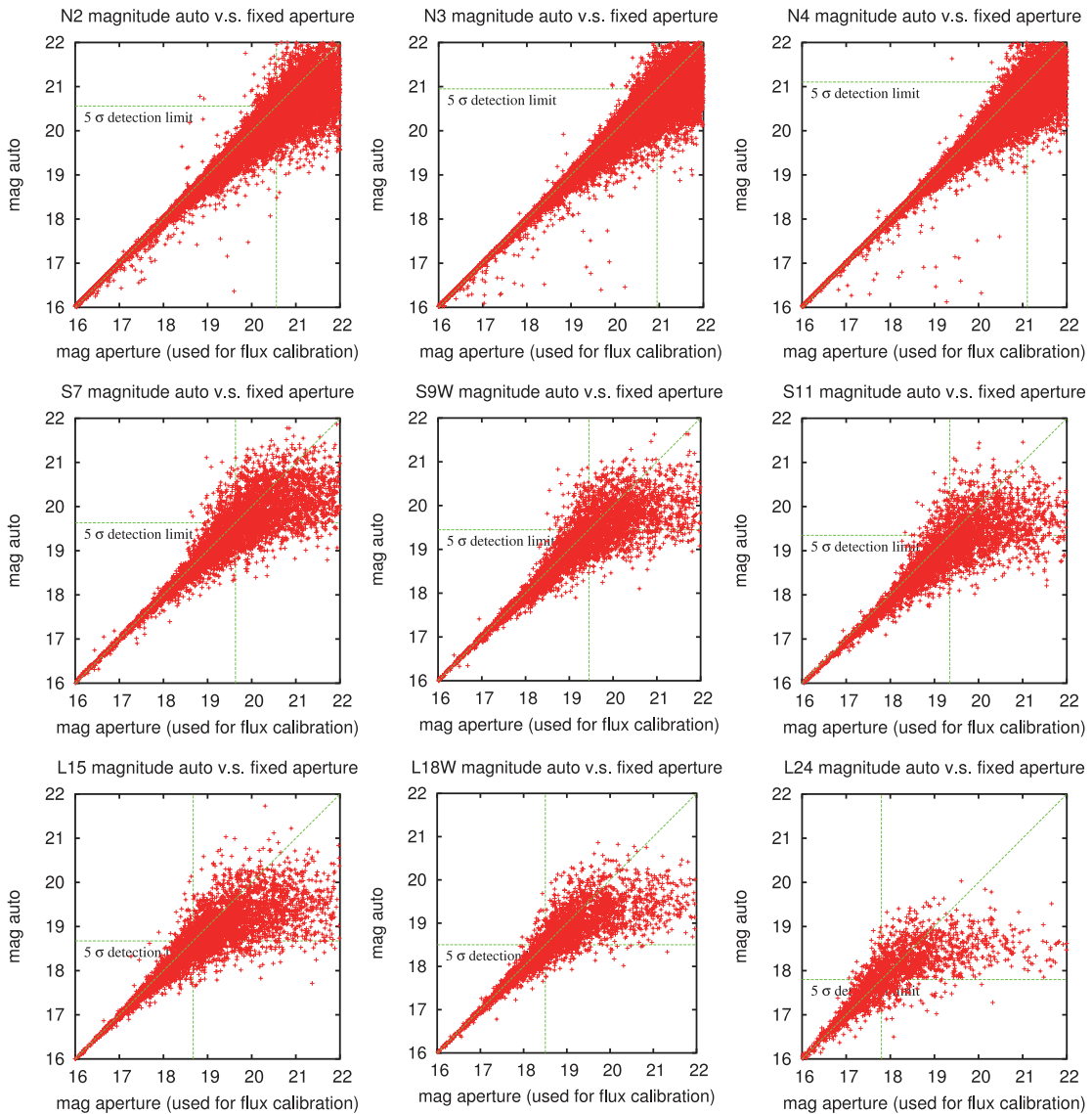§ Completeness limit.

Fig. 6. Magnitudes of individual sources given by MAGAUTO are compared with that or MAGAPER with the same aperture radius as the observations of the standard stars. No systematic difference between MAGAUTO and MAGAPER are seen above the 5 σ detection limit, although there are large systematic differences at fainter levels.
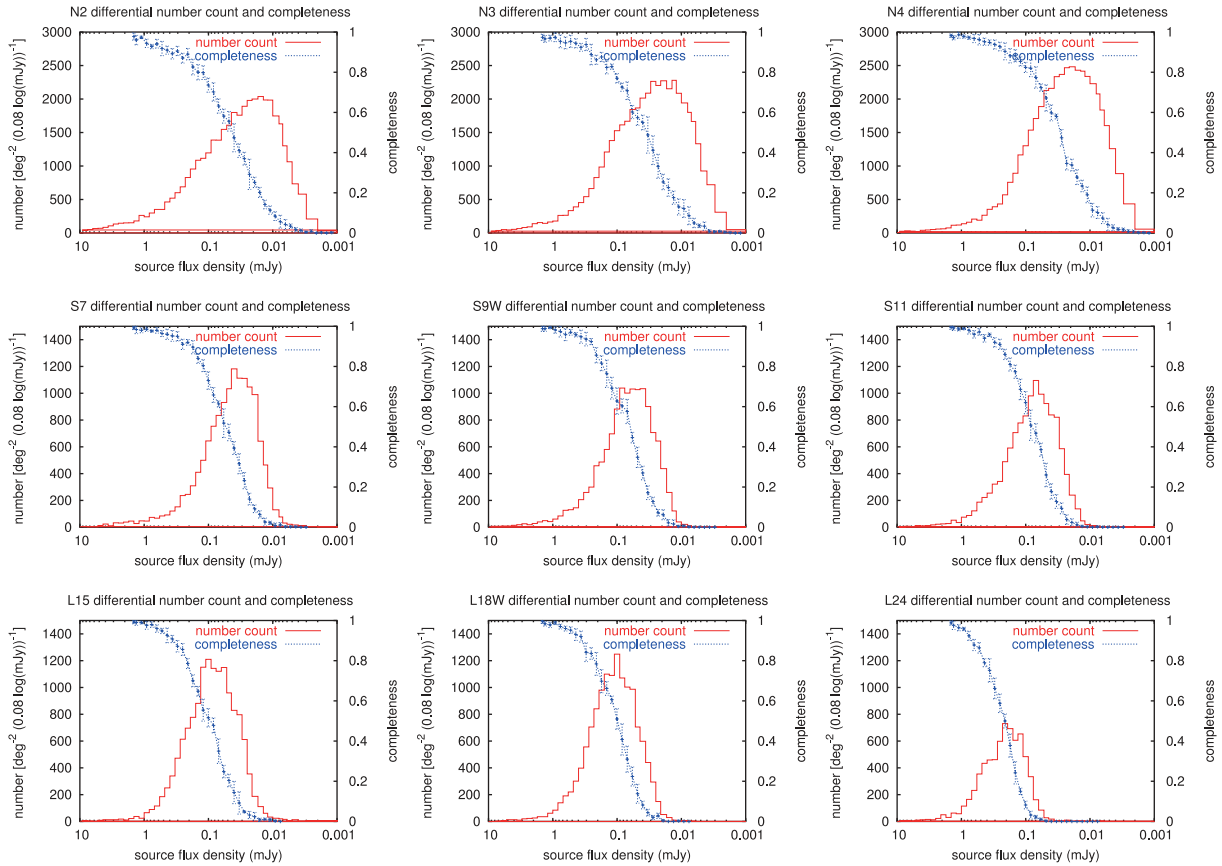
Fig. 7. Differential source counts and the result of the completeness estimates are shown for each band. The source counts include all sources extracted, and are not corrected for incompleteness. The bin size of the count is 0.2 magnitude (0.08 in log mJy). The effective area for the counts are listed in table 2.

overlaid on the AKARI/IRC images in figure 5. The magnitude zero point was derived by observations of standard stars, and is described in Tanabé et al. (2008).

Simple aperture photometry (Sextractor's MAGAPER) was also calculated in order to estimate the amount of aperture correction. The aperture radius was set to be the same as used in the standard star observations: 10 and 7.5 pixels in the NIR and MIR-S/L images, respectively. Figure 6 shows the comparison between the flux estimations by MAGAUTO and MAGAPER for each source. We did not apply any aperture correction for further analysis because the results using MAGAUTO and MAGAPER were reasonably consistent.

The number of sources detected in this extraction is summarized in table 2, and the differential number counts are shown in figure 7.

4.3. Astrometry

The accuracy of the astrometry was tested by comparing the source positions from the AKARI catalog with the 2MASS catalog. For each AKARI source, the 2MASS source which is closest to the AKARI source is identified as the counterpart, and then the offset of each AKARI source is derived. The spatial distribution of the offsets, the mean offsets, and the root mean square (RMS) offsets are shown in figure 8 and table 3.

Table 3. Accuracy of astrometry in arcsec.

Band	$\Delta\alpha$		$\Delta\delta$	
	Mean	RMS	Mean	RMS
N2	−0.027	0.397	−0.047	0.448
N3	−0.002	0.470	−0.016	0.486
N4	−0.010	0.528	−0.004	0.521
S7	−0.037	0.780	0.044	0.831
S9W	−0.058	1.086	0.108	1.034
S11	0.079	1.391	0.186	1.430
L15	0.042	1.840	0.173	1.896
L18W	0.111	1.894	0.455	1.896
L24	0.188	2.163	−0.051	2.278

The RMS is smallest at the N2 band ($0.''4$) and largest at the L24 band ($2.''2$). This is probably due to the larger probability of mis-identifications, resulting both from the very red optical–infrared colors of the MIR-L sources, and from larger size of the PSFs at longer wavelengths.
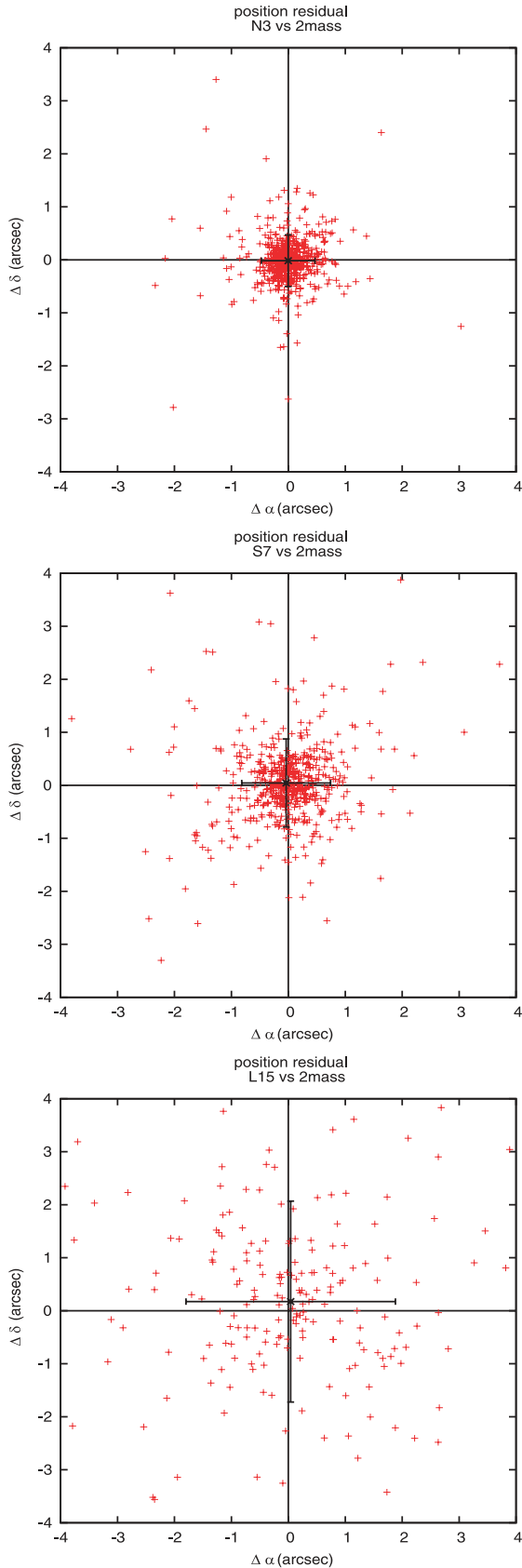
Fig. 8. Relative positions of the closest source in the 2MASS catalog for each detected source in AKARI catalog. The results at *N3*, *S7*, and *L15* bands are shown for example.

5. Sensitivity

5.1. Sky Noise Limit

The sensitivity of the point source extraction was estimated by measuring the fluctuations in the photometry at random blank sky positions. Positions close to sources were not used for this measurement in order to avoid source contamination.

We made simple aperture photometry at each random position using the IRAF/PHOT package (Tody 1986). No weighting, no PSF fitting, and no centering were performed. The size of aperture radius was set to 1.5 pixel for all nine bands. The apertures used are shown in figure 5.

In order to evaluate the fluctuations in the photometry, the histogram of the measurements was fit with a Gaussian distribution. We defined the one sigma level of the fluctuation as the standard deviation of the Gaussian. Finally, taking the aperture correction into account, we calculated a 5σ detection limit for a point source.

The 5σ detection limits are estimated to be 11.0, 48.9, and 117 μJy in the *N3*, *S7*, *L15* bands, respectively. The results of the detection limit estimation for all nine bands are summarized in table 4, together with the results of one pointed observation in the pilot survey (Wada et al. 2007).

5.2. Completeness Limit

The completeness of the source extraction was estimated via Monte Carlo simulations. We added artificial sources from a truth catalog into the final mosaicked images, and then extracted the sources again using the same extraction parameters. We then compared the position and magnitude of the input sources with the extracted sources. If there was an extracted source within 2 pixels around an input source, and provided the difference in magnitude between the input source and the extracted source was less than 0.5 magnitude, we regarded the event as a successful extraction of an artificial truth source. We define the completeness of the source extraction as the number of successfully extracted truth sources divided by the total number of artificial input sources that were originally added into the original image.

The calculation was performed by dividing our flux range into magnitude bins of size 0.2 magnitudes (i.e., uniform bin size, 0.08 in log Jy) and populating each bin with 20 artificial sources. The magnitude distribution of the sources was normalized to a flat Euclidian universe in each bin. These 20 sources were then added in random positions in the image, assuming a circular PSF. We did not insert a source if the minimum distance to another artificial source was less than 20 pixels, to avoid self-confusion effects among the artifical sources.

In order to improve the statistical significance of the Monte Carlo simulations, we performed 5 statistically independent calculations for each magnitude bin, creating an effective total of 100 artificial sources. The simulation was then subsequently carried out for each magnitude bin in turn. The results are shown in figure 7, and the completeness limits are summarized in table 4.

We also estimated the completeness of the survey using direct comparisons of detected sources with a deeper observation, as a check of the reliability of the Monte Carlo

Table 4. Detection limit (sky noise limit) and completeness limit in μJy.

Source	This work				Wada et al. (2007)(1 pt)				Factors of improvement			
Limit	Completeness			Detection	Completeness			Detection	Completeness			Detection
Criterion	30%	50%	80%	5σ	30%	50%	80%	5σ	30%	50%	80%	5σ
N2	23.5	42.5	145.2	14.2	—	—	—	—	—	—	—	—
N3	21.4	34.6	110.9	11.0	16.3	27.7	81.9	11.2	0.76	0.80	0.74	1.01
N4	17.1	29.0	77.4	8.0	—	—	—	—	—	—	—	—
S7	32.2	54.0	119.6	48.9	50.8	75.5	171.4	71.3	1.58	1.40	1.43	1.46
S9W	43.1	62.6	165.5	58.5	—	—	—	—	—	—	—	—
S11	51.2	80.7	166.4	70.9	—	—	—	—	—	—	—	—
L15	63.7	93.3	218.3	117.0	93.6	134.2	289.6	200.9	1.47	1.44	1.33	1.72
L18W	68.1	98.8	222.9	121.4	—	—	—	—	—	—	—	—
L24	157.7	209.8	450.4	275.8	—	—	—	—	—	—	—	—
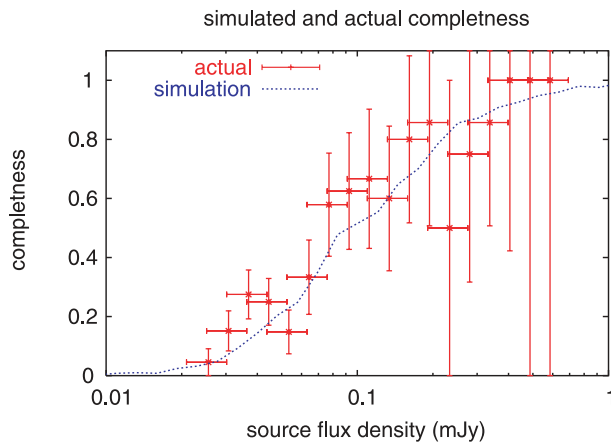
Fig. 9. Completeness estimates in the *L15* band from the Monte Carlo simulations and from direct comparison of sources (actual completeness) in the common area with a deeper observation (Wada et al. 2007). The horizontal error bars represent the bin size, and the vertical error bars represent statistical uncertainty, $\sqrt{N_{\mathrm{detection}}}/N_{\mathrm{input}}$.

Table 5. Source number density in units of sources per beam.

Filter	Number of source per beam*	FWHM of PSF in pixels	in arcsec
N2	1/29.7	3.0	4.4
N3	1/26.8	3.0	4.4
N4	1/26.1	3.0	4.4
S7	1/61.0	2.2	5.1
S9W	1/65.7	2.2	5.1
S11	1/69.0	2.2	5.1
L15	1/53.7	2.3	5.4
L18W	1/58.1	2.3	5.4
L24	1/112.2	2.3	5.4

* The radius of the beam is set to FWHM/2.35 of the PSF.

simulations. A part of this survey area was independently covered by the pilot survey (Wada et al. 2007) which had twice the exposure time per FOV than the NEP survey. We used this pilotsurvey for our completeness test. We define the actual completeness by the detection rate of source which are detected in the deeper observation. The calculation method is as same as that of the Monte Carlo simulations, but the input source list is the observed source list from the deeper observation. The results are consistent with those of the Monte Carlo simulations and are shown in figure 9.

5.3. Source Confusion

We calculated the source number density in units of sources per beam (table 5), to assess the effect of source confusion. In the case of the *N2*, *N3*, and *N4* bands, the density is nearly equal to 1/30, the classical limit of source confusion (Condon 1974; Hogg 2001). Clearly, these observations are limited by source confusion. In the case of bands from 7 to 18 μm, the density is still lower than the classical confusion limit. The *L24* band has

low density compared to the other bands. This is probably due to its comparatively poorer sensitivity caused by the narrower band width of the *L24* filter.

6. Discussion

6.1. Comparison with the Pilot Survey

6.1.1. Source number counts

In order to show the benefits of our "DEEP and WIDE" survey strategy, we have made a comparison of the number counts at 3, 7, and 15 μm with the results from the pilot survey (Wada et al. 2007) in figure 10. The counts from our survey show good agreement with the pilot survey of the faint end. At the bright end, our survey clearly has smaller scatter in the counts. This is due to the higher statistical significance obtained by the wide-area component of our survey.

6.1.2. Sensitivity

The limits of our survey are not as deep as we expected from the pilot survey. Because the average integration time

3μm count from LS NEP DEEP

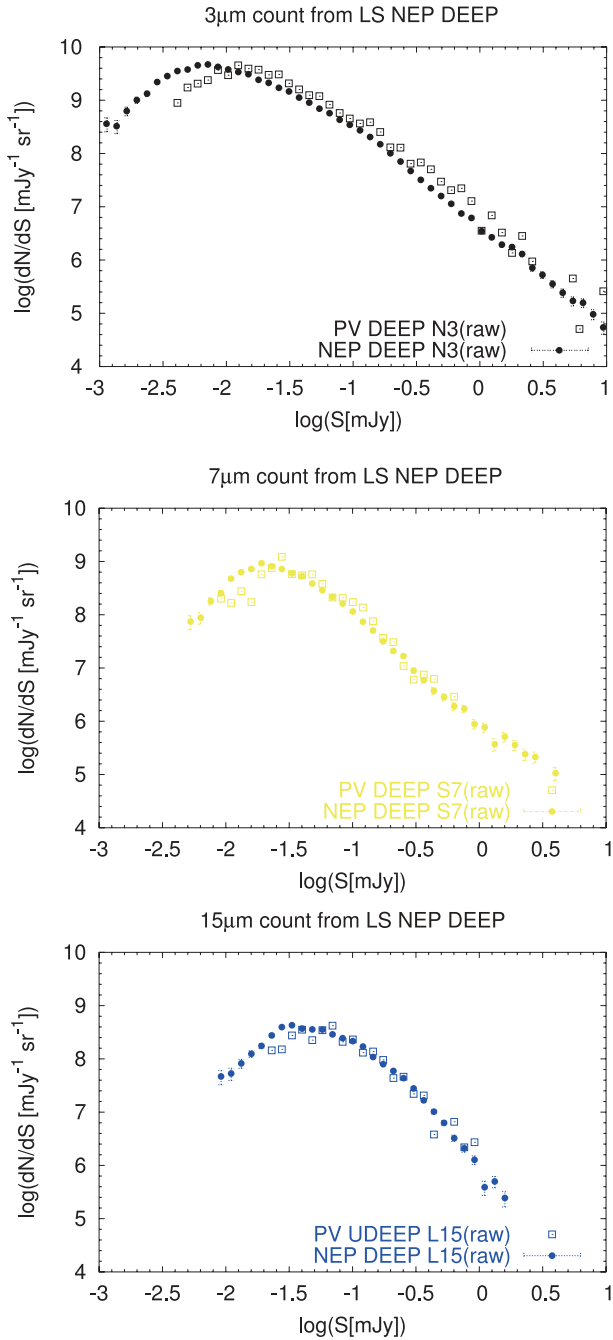**7μm count from LS NEP DEEP**

15μm count from LS NEP DEEP

Fig. 10. 3, 7, and 15 μm differential source counts are plotted together with the result from the pilot survey (Wada et al. 2007). The result is consistent with each other in the fainter end, while our survey has smaller scattering than Wada et al. (2007) because of its wideness.

of our survey corresponds to that of four pointed observations per field of view, simple statistics led us to expect a factor of 2 improvement in sensitivity compared to that for a single pointed observation.

In the *N2*, *N3*, and *N4* bands, the cause of this discrepancy is clearly due to the effects of source confusion. In the other bands, the cause is probably the differences of methods of image combines. Our survey used the "median combine" technique in order to reject spurious data, while the pilot survey used "average combine" with a sigma clipping using the noise model. Applying the "average combine" will improve the sensitivity by a factor of one and half. Unfortunately, the `Swarp` software does not have any capability for clipping out spurious event in "average combine". Software must be developed for the further improvement of our survey sensitivity.

7. Summary

We have made a deep and wide imaging survey with all 9 AKARI/IRC bands from 2 to 24 μm in the North Ecliptic Pole region. The survey has covered a circular area of 0.38 deg^2 where a deep optical multi-band survey has been finished by Subaru/Suprime-Cam.

The 5 σ point source sensitivities of the survey are 14.2, 11.0, 8.0, 48, 58, 71, 117, 121, and 275 μJy at the wavelengths of 2, 3, 4, 7, 9, 11, 15, 18, and 24 μm, respectively. The survey is limited by sky noise at wavelengths from 7 to 24 μm, while 2 to 4 μm are limited by source confusion.

We have also made a point source catalog consisting of more than 5000 sources with a 50% completeness limits of 93 μJy at 15 μm. Our source counts are consistent with the pilot survey (Wada et al. 2007) at the faint end and have better statistical significance at the bright end.

Further improvements of sensitivity, especially for the mosaicked images in the MIR-S and MIR-L bands, might be possible by using clipped "average"method instead of "median" method in the image combining process.

References

Alonso-Herrero, A., et al. 2006, ApJ, 640, 167
Bertin, E., & Arnouts, S. 1996, A&AS, 117, 393
Caputi, K. I., et al. 2006, ApJ, 637, 727
Condon, J. J. 1974, ApJ, 188, 279
Fazio, G. G., et al. 2004, ApJS, 154, 10
Franceschini, A., et al. 2006, A&A, 453, 397
Furusawa, H., et al. 2008, ApJS, 176, 1
Genzel, R., & Cesarsky, C. J. 2000, ARA&A, 38, 761
Giavalisco, M., et al. 2004, ApJ, 600, L93
Hogg, D. W. 2001, AJ, 121, 1207
Houck, J. R., et al. 2004, ApJS, 154, 18
Imai, K., Matsuhara, H., Oyabu, S., Wada, T., Takagi, T.,
    Fujishiro, N., Hanami, H., & Pearson, C. P. 2007, AJ, 133, 2418
Kashikawa, N., et al. 2004, PASJ, 56, 1011
Kessler, M. F., et al. 1996, A&A, 315, L27
Lee, H. M., et al. 2007, PASJ, 59, S529
Lee, H. M., et al. 2008, PASJ   submitted
Le Floc'h, E., et al. 2005, ApJ, 632, 169
Matsuhara, H., et al. 2006, PASJ, 58, 673
Matsuhara, H., et al. 2007, PASJ, 59, S543
Murakami, H., et al. 2007, PASJ, 59, 369
Narae, H., et al. 2007, ApJS, 172, 583
Negrello, M., et al. 2008, MNRAS   submitted
Neugebauer, G., et al. 1984, ApJ, 278, L1
Oliver, S., et al. 2002, MNRAS, 316, 749
Onaka, T., et al. 2007, PASJ, 59, S401
Pérez-González, P. G., et al. 2008, ApJ, 675, 234
Rieke, G. H., et al. 2004, ApJS, 154, 25
Scoville, N., et al. 2007, ApJS, 172, 1
Skrutskie, M. F., et al. 2006, AJ, 131, 1163
Takagi, T., et al. 2007, PASJ, 59, S557
Takagi, T., & Pearson, C. P. 2005, MNRAS, 357, 165
Tanabé, T., et al. 2008, PASJ, 60, S375
Tody, D. 1986, Proc. SPIE, 627, 733
Wada, T., et al. 2007, PASJ, 59, S515
Werner, M. W., et al. 2004, ApJS, 154, 1